Journal of Magnetism and Magnetic Materials 322 (2010) 523–529

Contents lists available at ScienceDirect

Journal of Magnetism and Magnetic Materials

journal homepage: www.elsevier.com/locate/jmmm

Specific heat investigation on the magnetic phase diagrams of RNi$_2$B$_2$C (R = Gd, Er)

M. ELMassalami [a,*], R.M. Saeed [a], C.M. Chaves [a], H. Takeya [b], M. Doerr [c], H. Michor [d], M. Rotter [e]

[a] Instituto de Fisica-UFRJ, CxP 68528, 21941-972, Rio de Janeiro, Brazil
[b] National Institute for Materials Science, 1-2-1 Sengen, Tsukuba, Ibaraki 305-0047, Japan
[c] Institut für Festkörperphysik, Technische Universität Dresden, D-01062 Dresden, Germany
[d] Institut für Festkörperphysik, Technische Universität Wien, A-1040 Wien, Austria
[e] University of Oxford, Department of Physics, Clarendon Laboratory, Parks Road, Oxford OX1 3PU, UK

ARTICLE INFO

Article history:
Received 24 June 2009
Received in revised form
25 August 2009
Available online 9 October 2009

PACS:
74.72.Ny
75.30.Ds
75.30.Kz
75.40.Cx

Keywords:
Borocarbides
Specific heat
Magnetic phase diagrams

ABSTRACT

The borocarbides RNi$_2$B$_2$C (R = magnetic rare earth) exhibit rich H–T magnetic phase diagrams. Using field-dependent specific heat measurements on single-crystals of RNi$_2$B$_2$C (R = Gd, Er), this work investigated the magnetic contribution to the specific heat when T and H are varied across these H–T phase diagrams. These measurements, together with the ones reported on HoNi$_2$B$_2$C, confirm that the overall evolution of each $C_{mag}(T,H)$ curve is a faithful reflection of the features observed in the corresponding phase diagram: in particular the successive field-induced metamagnetic modes, appearing in the reported magnetization $M(T,H)$ curves, are also manifested in these $C_{mag}(T,H)$ curves, just as required by the Maxwell identity $(\partial C_{mag}/\partial H)_T = T(\partial^2 M/\partial T^2)_H$. Within the lower ranges of temperature and fields, the calculations based on linearized field-dependent spin-wave theory are found to reproduce satisfactorily the measured $C_{mag}(T,H)$ curves: accordingly, within these ranges, the thermodynamical properties of these compounds can be rationalized in terms of only two parameters, namely, the spin-wave energy gap and the stiffness coefficient. Based on the satisfactory agreement between theory and experiment, we are able to provide an explanation for the plateau like behavior observed in, say, the $M(T,H)$ isotherms. Finally, for the particular case of GdNi$_2$B$_2$C wherein the anisotropy is dictated solely by the classical dipole interactions, the main features of its $C_{mag}(T,H)$ are found to be reproduced by numerical calculations based on the model of Jensen and Rotter [Phys. Rev. B 77 (2008) 134408].

1. Introduction

The H–T magnetic phase diagrams of the heavy members of the intermetallic RNi$_2$B$_2$C (R = rare earth) magnets are characterized by a cascade of metamagnetic transformations, higher Neel points T_N, and stronger saturation fields, H_{sat} (see Refs. [1,2] and references therein). Both T_N and H_{sat} are well scaled by de Gennes factors testifying to the involvement of the indirect exchange coupling mechanism [3]. Moreover, except for GdNi$_2$B$_2$C, there are strong anisotropic forces and the competition between these forces and the exchange interaction is one of the main driving mechanisms behind the characteristic features of their magnetic phase diagrams [1,2]. In general, the role of these competing forces is analyzed in terms of a Hamiltonian that consists of bilinear exchange, single-ion crystalline electric field (CEF), and dipolar interactions: calculations based on such a Hamiltonian yield H–T phase diagrams that are in reasonable agreement with experiments on, say, HoNi$_2$B$_2$C [4,5], GdNi$_2$B$_2$C [6,7], and ErNi$_2$B$_2$C [8].

The zero-field magnetic structures of the RNi$_2$B$_2$C compounds can be divided into two broad classes [9]: (i) the equal-amplitude, collinear, and commensurate AFM structures (R = Pr, Nd, Dy, Ho ($T \leq 5$ K)): with the exception of Pr wherein $k = (0.5, 0, 0.5)$, their moments are coupled ferromagnetically within the layers which are, in turn, antiferromagnetically stacked on each other along the c-axis: $k = (0, 0, 1)$, and (ii) the amplitude-modulated, incommensurate structures [R = Gd, Tb, Ho ($5 < T < 6.3$ K), Er, Tm]; on lowering the temperature, these modulated structures are gradually transformed into an equal-amplitude [squared-up spin-density] states. HoNi$_2$B$_2$C is a particular case wherein three magnetic modes are manifested [9]: a c-axis incommensurate spiral, $k_1 = (0, 0, 0.91)$, emerges below 8.5 K while an a-axis incommensurate state, $k_2 = (0.55, 0, 0)$, develops below 6.3 K. Finally, below 5 K, both of the incommensurate states are substituted by a commensurate antiferromagnetic structure with $k_3 = (0, 0, 1)$.

* Corresponding author.
E-mail address: massalam@if.ufrj.br (M. ELMassalami).

0304-8853/$ - see front matter © 2009 Elsevier B.V. All rights reserved.
doi:10.1016/j.jmmm.2009.10.009

On applying an external magnetic field along the easy-axis of the ordered states of most RNi$_2$B$_2$C magnets, both of the commensurate and incommensurate modes are observed to undergo a cascade of magnetic phase transformations leading to a set of different magnetic modes; each having a distinct propagation vector and a distinct total magnetic moment. For the case of, say, HoNi$_2$B$_2$C and ErNi$_2$B$_2$C, there emerges a very rich and interesting H–T magnetic phase diagram [10–12] with characteristic features that are reflected in all measured thermodynamical properties. As an example, the low-temperature magnetization isotherms show a cascade of step-like metamagnetic phase transformations with constant plateau between the consecutive transformations [13–17]. As the low-temperature magnetic properties are governed by the excitation spectra of the magnon quasiparticles then, according to the spin-wave theory, the surge of such stair-like features is a manifestation of related field-dependent distinct features in the dispersion relations or density of states of the magnon quasiparticles. Then a spin-wave analysis of the H- and T-dependence of the thermodynamical properties would contribute to the understanding of the magnetic phase diagrams and the related thermodynamical properties of these borocarbides. Using field-dependent specific heat measurements on single-crystals of RNi$_2$B$_2$C (R = Gd, Er), this work investigated the magnetic contribution to the specific heat when T and H are varied across these H–T phase diagrams.

The magnetic structures of the compounds under study are well established for the high- and low-field part of their phase diagram: within the intermediate-field range, the structures are either unknown or too complex which in turn hinders the construction of an analytical expression for the dispersion relations and consequently the magnon specific heat contribution. Furthermore, it happened that the highest magnetic field available for this study is lower than the one needed to reach the high-field saturated state. Accordingly, the comparison of the measured and calculated magnetic specific heats (the latter is based on spin-wave theory) was carried out only for the lower field limit (Sections 2.2 and 4.3). For the intermediate-field range (as well as across the available H–T plane of the phase diagram), basic thermodynamical relations were employed to relate the field evolution of the measured magnetic specific heat to the temperature dependence of the isofield magnetization curves (Section 5). Finally, since the linearized magnon theory is applicable only for the lower temperature range, mean-field model calculations were carried out to evaluate the magnetic specific heat within the higher range of the ordered state; this part of the study was restricted to only GdNi$_2$B$_2$C (Sections 2.2 and 4.3.1.2): in contrast to R = Er and Ho [18], GdNi$_2$B$_2$C has negligible crystalline field anisotropy and as such the classical dipole interactions play a crucial role in shaping its magnetic structure.

2. Theoretical background

As mentioned above, three approaches will be used to analyze the field and temperature dependence of the measured $C_{mag}(T,H)$ curves: (i) basic thermodynamical analysis which allows us to relate the evolution of $C_{mag}(T,H)$ to that of the magnetization measurements: thus permitting a generalization to field and temperature ranges beyond the limitation of our experimental setups, (ii) the linearized spin-wave analysis which allows us to investigate the low-temperature, low-field range, and (iii) mean-field model calculation based on which we will be able to probe the higher temperature region, a region which is not accessible to spin-wave analysis.

2.1. Field-dependent magnon specific heat of RNi$_2$B$_2$C

A theoretical expression for the description of the zero-field $C_{mag}(T,H)$ of the AFM-ordered borocarbide have been reported previously [19]. Along similar theoretical considerations we calculated the field-dependent $C_{mag}(T,H)$ of these AFM samples for the low-field limit wherein the applied field is lower than that of the spin flop field ($H < H_{sf}$). The external field H is applied at angle θ away from the easy axis. Then at the low-temperature limit, $C_{mag}(T,H)$ is found to be

$$C_{mag}(T,H) = R\Delta_a^4/(4\pi^2 D_a^3 T^2) \sum_{m=1}^{\infty} \{T\cosh(m\xi/T)[K_4(m\Delta_a/T) + \langle 1+2\xi^2/\Delta_a^2\rangle K_2(m\Delta_a/T)] - 0.5m\xi\sinh(m\xi/T)[K_4(m\Delta_a/T) - K_0(m\Delta_a/T)]\}, \quad (1)$$

where $K_n(m\Delta_a/T)$ represents the modified Bessel function of the second kind, $\xi = g\mu_B H\cos(\theta)/k_B$ (J, $g = g_J$, μ_B, and k_B have their usual meanings). In this expression, the only fit parameters are D_a and Δ_a: D_a is a measure of the stiffness and is given by

$$D_a = [16(\mathcal{J}_0+\mathcal{J}_1)\mathcal{J}_0 J^2 + 2\mathcal{J}_0 J(g\mu_B H_a)]^{1/3} \cdot (4\mathcal{J}_1 J)^{1/3}, \quad (2)$$

where $\mathcal{J}_0$ and $\mathcal{J}_1$ are effective exchange couplings among the nearest neighboring moments within, respectively, the same plane and within neighboring planes. $\vec{H}_a$ is a measure of the magnetic anisotropy while the two distinct field-dependent energy gaps $\Delta^{\pm}(H)$ are given by (in the limit of low temperature)

$$\Delta^{\pm}(H) = +\sqrt{(g\mu_B H_a)^2 + 16\mathcal{J}_1 g\mu_B J H_a} \pm g\mu_B H\cos(\theta) = \Delta_a \pm g\mu_B H\cos(\theta). \quad (3)$$

Evidently $\Delta^{\pm}(H)$ do not depend on $\mathcal{J}_o$ and their separation is linearly related to $H\cos(\theta)$. Due to the type of the undertaken approximations, Eq. (1) does not hold when $H\cos(\theta)$ is equal to or higher than the spin-flop field, H_{sf}, which is the value at which the lower branch goes to zero. The field influence on Eq. (1) enters only through $H\cos(\theta)$. Furthermore, this equation reduces to Eq. (25) of Joenk [20] when $\mathcal{J}_0 = \mathcal{J}_1$ and it gives the well-known T^3 relation when $k_B T \gg \Delta_a$ [21].

For $T \to 0$, $\Delta_a/T \to \infty$; then, if $\xi < \Delta_a$, Eq. (1) reduces to:

$$C_{mag}(T,H) \simeq \frac{R\Delta_a^{7/2}}{2^{1/2}\pi^{3/2}D_a^3 T^{1/2}} \exp\left(\frac{\xi-\Delta_a}{T}\right)\left[1 - 2\frac{\xi}{\Delta_a} + \left(\frac{\xi}{\Delta_a}\right)^2 ..\right] \quad (4)$$

indicating a dominant exponential character within this H–T region.

From above, it is evident that the applied field tends to remove the degeneracy appearing in Eq. (3). As a consequence, the fractional contribution of the lower mode to $C_{mag}(T,H)$ increases leading to $(\partial C_{mag}/\partial H)_T > 0$. On the other hand, for $H \to H_{sat}$, an increase in H would induce a gradual decrease in $C_{mag}(T,H)$ resulting in $(\partial C_{mag}/\partial H)_T < 0$. Similar arguments hold for $M(T,H)$.

2.2. Mean-field model calculation of $C_{mag}(T,H)$ of GdNi$_2$B$_2$C

The above calculations of the magnon $C_{mag}(T,H)$ of RNi$_2$B$_2$C compounds are valid only within the lower temperature range, mostly around liquid helium temperatures. To investigate the magnetic contribution across the whole magnetically ordered range, we resort to mean-field model calculations applied on the simpler case of the ordered $^{7/2}S$–moments of GdNi$_2$B$_2$C. Jensen and Rotter [7] showed that a model consisting of a sum of the bilinear Heisenberg exchange term and the classical dipole interaction is able to explain (i) the features of the whole magnetic phase diagram, (ii) the so-called magnetoelastic paradox [22], and (iii) the zero-field $C_{mag}(T)$ of GdNi$_2$B$_2$C. Here, in this

work, their calculations of $C_{mag}(T,H)$ are extended to fields up to $H \leq 80$ kOe using the McPhase program package (www.mcphase.de) [23].

3. Experimental

The RNi$_2$B$_2$C (R = Gd, Er) single-crystals, together with R = Ho [18], were selected for this study because they offer a good representation of the magnetic properties of the whole RNi$_2$B$_2$C series: ErNi$_2$B$_2$C and GdNi$_2$B$_2$C are good representatives of the modulated, incommensurate magnetic structures; the anisotropic forces are stronger in the former [24] while extremely weaker in the latter [25,26]. It is recalled that HoNi$_2$B$_2$C is a typical representative of the collinear, commensurate, AFM structures.

The single crystals of these three representatives compounds, together with that of the reference YNi$_2$B$_2$C, were grown by floating zone method [27]. Results from extensive structural and physical characterizations are in good agreement with the reported data, confirming the good quality of our crystals. The temperature-dependent specific heat at fixed fields was measured on two different setups. One is pulse-type adiabatic calorimeter [500 mK $< T <$ 25 K, 120 kOe] and the second is a quasi-adiabatic setup with a temperature range covering 1.5–100 K and a field up to 80 kOe.

4. Results and discussion

4.1. Electronic and lattice contribution

For all compounds, the total specific heat C_{tot} was analyzed as a sum of an electronic C_e, a phonon C_{ph}, a nuclear C_n, and a magnetic contribution C_{mag}:

$$C_{tot} = C_e + C_{ph} + C_n + C_{mag}. \quad (5)$$

Both C_e and C_{ph} are calculated based on the analysis of the specific heat of the isomorphous single-crystal YNi$_2$B$_2$C. As $C_M(T)$ of the studied compounds are much larger than $C_e + C_{ph}$, then $C_M(T)$ would not be noticeably modified even if we take the bare values of YNi$_2$B$_2$C. Specifically, instead of estimating C_{ph} directly from that of YNi$_2$B$_2$C [28], we tried other means (such as mass normalization [29] or using other nonmagnetic isomorphs [28,30]). We found out that, irrespective of the estimation method, the obtained spin-wave fit-parameters are differing by only a few percent: other than this weak variation, the use of different estimation processes does not influence the conclusions drawn from this work.

The low-temperature electronic contribution was estimated as follows: while the normal-state contribution was evaluated from that of the single-crystal YNi$_2$B$_2$C (the same as that used in Ref. [28]), the contribution within the superconducting region was evaluated as $3\gamma T^3/T_c^2$. As LuNi$_2$B$_2$C and YNi$_2$B$_2$C have almost the same γ [30], then it is reasonable to consider γ of the heavy members of RNi$_2$B$_2$C to be equal.

Within the normal state (or $H > H_{c2}$ if applicable), the electronic, phononic or nuclear contributions are taken to be field independent (see below). The various zero-field contributions of RNi$_2$B$_2$C (R = Gd, Ho, Er) were illustrated in, e.g., Ref. [28].

4.2. Nuclear contribution

The magnetic contribution was obtained as follows: after subtracting the electronic and phonic contribution by the process explained in Section 4.1, the resultant ($C_{tot} - C_e - C_{ph}$) is confronted with the sum of the calculated nuclear and magnetic (Eq. (1)) terms. $C_n(T)$ was obtained after diagonalizing the nuclear Hamiltonian (see e.g. Refs. [31,32]).

The least square fit involves the simultaneous search for the best values of the five parameters, namely the nuclear parameters Λ_{iso}, α_{int}, and P as well as the spin-wave parameters Δ_a and D_a (see below). The fit does reproduce satisfactorily the measured nuclear specific heat of ErNi$_2$B$_2$C and HoNi$_2$B$_2$C [18] (GdNi$_2$B$_2$C has no nuclear contribution): Table 1 give the best-fit parameters. It is evident from Table 1 that α_{int} of the studied R^{3+} compounds are close to the values reported for the corresponding rare-earth metals [31,32] indicating that the hyperfine field is determined mainly by the internal electronic configuration of the R^{3+} ion. On the other hand, the P parameters are extremely small; this is not surprising since the point group of the sites at which the R^{3+} nucleus resides is D_{4h} in borocarbides and D_{6h} in the elemental rare earth. Finally, α_{ext}, associated with the externally applied magnetic field, is extremely small if compared to the internal field: for, say, ErNi$_2$B$_2$C [32], $H_{int} \approx 7 \times 10^6$ Oe and thus the highest applied field in this study is only $\sim 1\%$ of this H_{int}.

4.3. Magnetic contribution

Based on the general features of the $C_{mag}(T,H)$ curves (see e.g. Figs. 1 and 4, one distinguishes four temperature regions: (i) a paramagnetic region, $T > T_N(H)$, wherein $C_{mag}(T,H)$ is due to change in the population of the crystal field levels, (ii) a critical region, $T \approx T_N(H)$, wherein $C_{mag}(T,H)$ is related to critical phenomena, (iii) an intermediate region, $T_X < T < T_N$ ($T_X = T_R$ for GdNi$_2$B$_2$C or T_{WFM} for ErNi$_2$B$_2$C) which encompasses the sine-modulated states. Within this region, the spin-wave analysis of Section 2.1 is not applicable. Finally (iv) the low–temperature region. For the range $T < \Delta_a$ and $H < H_{sf}$ (none of the applied fields on the compounds under study satisfies the inequality $H > H_{sat}$), the collinear AFM/squared-up states are established and therefore the measured $C_{mag}(T,H)$ can be confronted with Eq. (1). It is worth mentioning that for extremely low-temperatures ($T \ll \Delta_a$), the exponential decaying character of $C_{mag}(T,H)$ (see Eq. (4)) and the relatively large contribution of the nuclear Schottky contribution

Table 1
The nuclear hyperfine parameters and the spin-wave parameters (Δ_a and D_a) of ErNi$_2$B$_2$C and HoNi$_2$B$_2$C (for the latter, these values are improvements on Ref. [18]).

RNi$_2$B$_2$C	Temp. range (K)	Λ_{iso} (%)	I	α_{int} (K)	P (mK)	Δ_a (K)	D (K)
HoNi$_2$B$_2$C	[0.5, 1.5]	100	7/2	0.362	−9.6	7.7 ± 0.3	4.6 ± 0.2
Ho metal [31]	[0.03, 0.5]		7/2	0.32	7.0		
ErNi$_2$B$_2$C	[0.1, 0.5]	90(5)	7/2	0.054	2.9	7.0 ± 0.1	3.0 ± 0.1
Er metal [32]	[0.03, 0.8]		7/2	0.042	−2.7		

The expression of $C_n(T)$ depends on the isotope abundance, Λ_{iso}, the magnetic dipole parameter, α_{int}, the electric quadrupole interaction parameter, P, and of course, the total nuclear spin I [31,32]. The parameters are obtained after fitting the experimental ($C_{tot} - C_e - C_{ph}$) curves to a sum of the nuclear and magnetic (Eq. (1)) terms. The specified temperature range indicates the region wherein the nuclear contribution is dominant (for the temperature range of the fit see Sections 4.3.2 and 4.3.3). The obtained nuclear parameters are compared with the corresponding parameters of the R-metal (see text).

set a lower temperature limit for the usefulness of the magnon analysis.

4.3.1. $GdNi_2B_2C$

The zero-field magnetic structure of $GdNi_2B_2C$ ($T_N = 19.5$ K) is an incommensurate sine-modulated structure (moments along b-axis and $k = 0.551a^*$) [25,33,34]. At $T_R \approx 13.5$ K, a moment reorientation sets-in leading to an additional modulated mode transversely polarized and having a small amplitude along the c-axis [33,34]. Two H–T phase diagrams were reported [26]: one for $H\|a$ and another for $H\|c$. The phase diagram for $H\|a$ shows three field-induced magnetic phase transitions [see inset of Fig. 1(a)]: (i) the saturation boundary at H_{sat}; (ii) the reorientation boundary at $H_R^{\|a}$; and finally (iii) the domain-wall [26] (or double-single q [7]) boundary at $H_D^{\|a}$. In contrast, the phase diagram for $H\|c$ shows only two transitions [see inset of Fig. 1(b)]: $H_{sat}^{\|c}$ (which is similar to $H_{sat}^{\|a}$) and $H_R^{\|c}$ (which is different from $H_R^{\|a}$). None of the two phase diagrams shows those characteristic H-induced cascade of metamagnetic phase transitions which are common in, say, the case of $R =$ Er, Ho; this is attributed to the absence of strong anisotropic features.

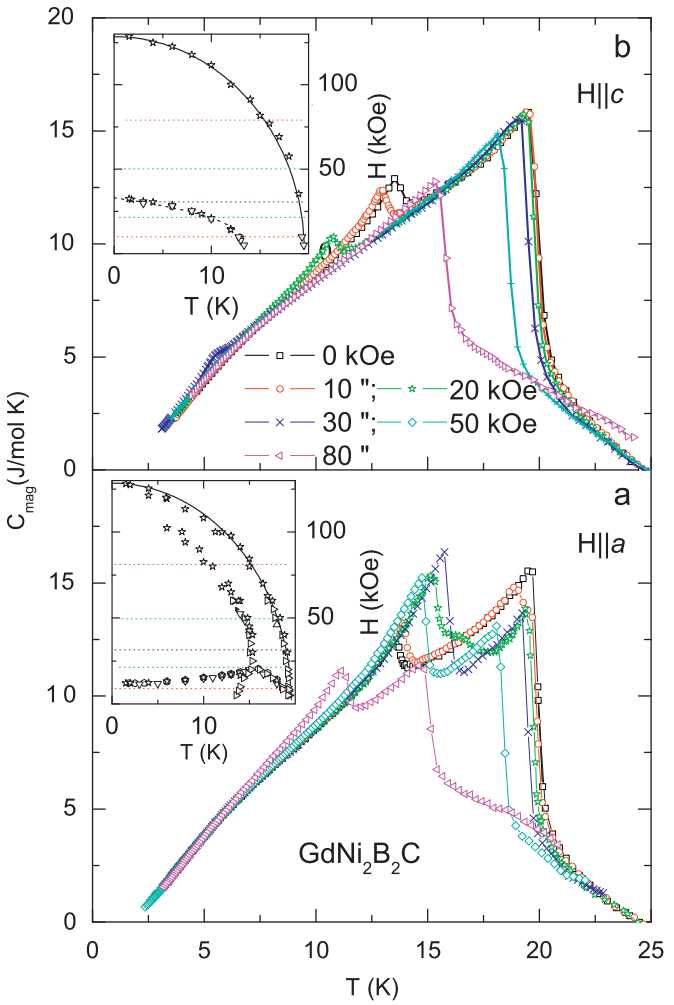

Fig. 1. (Color online) The isofield $C_{mag}(T,H)$ of $GdNi_2B_2C$ at various magnetic fields applied along: (a) $H\|a$ and (b) $H\|c$. The inset at the bottom-left (top-left) illustrates the H–T phase diagram for $H\|a(H\|c)$ [26]; there, the horizontal dotted lines represent the fields that were applied during these measurements. Evidently, both $H_R^{\|c}$ and $H_R^{\|c}$ anomalies in the C_{mag} (T,H) curve do reproduce the boundaries of the phase diagrams, in particular the reentrant feature appearing for the $H\|a$ case (see text).

As mentioned above, the experimental magnetic specific heat of $GdNi_2B_2C$ would be confronted with two model calculations: (a) the magnon calculation which is valid for sub-helium temperature (Section 2.1) and (b) the model calculations of Jensen and Rotter [7] which are extended from the helium-temperature range up to T_N (Section 2.2).

4.3.1.1. Magnon contribution to $C_{mag}(T,H)$. Fig. 1 shows that the most prominent features of $C_{mag}(T,H)$ of $GdNi_2B_2C$ are (i) the characteristic and distinct evolution of the $H_{sat}(T)$ and $H_R(T)$ curves and that (ii) within a certain region of T and H, $C_{mag}(T,H)$ appears to be hardly influenced by H. The cause of this apparent collapse of the $C_{mag}(T,H)$ curves becomes clear if we compare these curves with the predictions of Eq. (1): Fig. 2 shows a fit of the measured $C_{mag}(T,H=0)$ curve to Eq. (1) and the obtained fit parameters are $\Delta_a = 2.9 \pm 0.1$ K and $D = 5.6 \pm 0.1$ K which are close to the values reported in Ref. [19]. As both Δ_a and D_a are field independent, then the insertion of these values into Eq. (1) leads to the calculated $C_{mag}(T,H)$ curves (with no adjustable parameters) for all fields up to $H < k_B\Delta_a/(g\mu_B) \sim 20$ kOe (which is the field above or equal to which the magnon calculations based on Eq. (1) are not valid). Evidently the calculated and measured curves collapse on each other when $(T/\Delta_a \to 1)$: thus the apparent collapse is a reminder that our experimental conditions are good only for probing that part of the phase diagram wherein the field has a weak influence on the strongly exchanged-coupled AFM-like state. It is worth mentioning that this collapse is reflected also, by virtue of Eq. (6b), in the low-temperature $M(T,H)$ curves [25,26].

Fig. 1 shows also that the field-evolution of the low-temperature $C_{mag}(T,H_{\|c})$ curves is similar to that of $C_{mag}(T,H_{\|a})$ ones; the only difference is that all values of $H_{\|a}$ are lower than $H_R^{\|a}(T<T_R)$ boundary while, in contrast, some of the applied $H_{\|c}$ values are higher than $H_R^{\|c}(T<T_R)$ (see above); then it is no surprise that the presence of the $T_R(H_{\|c})$–event in $C_{mag}(T,H_{\|c})$ is more pronounced than in $C_{mag}(T,H_{\|a})$; in fact there is no manifestation of the reorientation event in the isofield $C_{mag}(T,H_{\|c}>32$ kOe) curves while, in contrast, for $H\|a$, the presence of the reorientation event is evident in all applied field

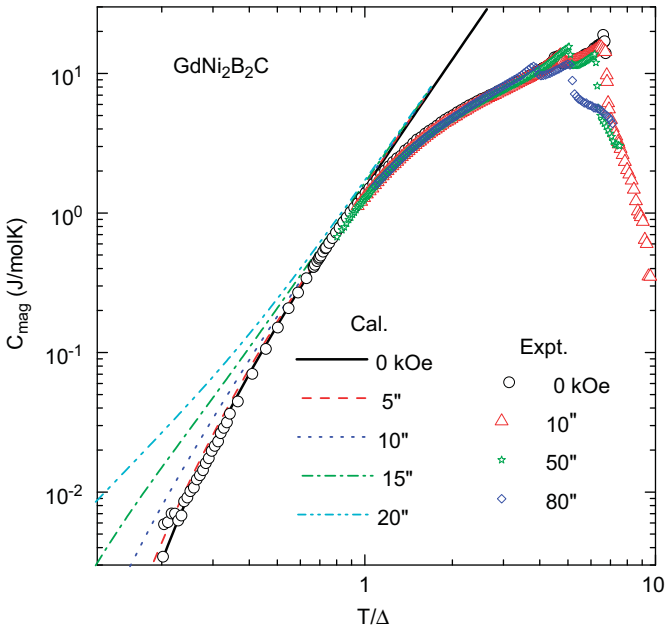

Fig. 2. (Color online) Log–log plot of C_{mag} versus the normalized temperature (T/Δ) under different applied fields $(H\|a)$. Symbols denote measurements while lines represent the calculated $C_{mag}(T,H)$ based on Eq. (1) (see text).

up to the maximum 80 kOe (see insets of Fig. 1). It is noted that the reentrant feature of the $H_R^{\|a}(T)$ curve within the neighborhood of 15 K is well evident in the $C_{mag}(T,H_{\|a})$ curves: as $H\|a$ is increased, the peak associated with this event moves first to higher temperature but reverts to a decreasing tendency when $H_{\|a}$ reaches values higher than 30 kOe.

Within $T<5$ K and $H_{\|a}<H_R(T)$ range, $(\partial S_{mag}/\partial H)_T$, $(\partial C_{mag}/\partial H)_T$, and $(\partial M/\partial T)_H$ (Ref. [25,26]) are weak but positive. Similar features are evident for the $H\|c$ case. When $H_{\|c}\to H_R(T)$, $C_{mag}(T,H_{\|c})$ is observed to increase, reaching a maximum at the phase boundary. A further increase in $H_{\|c}>H_R(T<T_R)$ leads to $(\partial C_{mag}/\partial H)_T<0$ indicating a decrease in the entropy and as such an increase in the ordered component along the c-axis. For $T>T_R$, both $(\partial M/\partial T)_H$ [Refs. [25,26]] and $(\partial C_{mag}/\partial H)_T$ are weak and positive for $H<30$ kOe but negative for 30 kOe $<H<H_{sat}$.

4.3.1.2. Model calculation of $C_{mag}(T,H)$. Fig. 3 compares the measured magnetic specific heat of $GdNi_2B_2C$ with the model calculation of Jensen and Rotter (see Section 2.2). [7] It is noted that, even though there are no adjustable parameters (other than the experimental T_N) in these calculations, the model is able to reproduce the main features of the measured $C_{mag}(2\,\mathrm{K}<T<T_N)$ for both $H_{\|a}\le 80$ kOe and $H_{\|c}\le 80$ kOe [see, respectively, Fig. 3(a) and (b)]. The following achievements of the model calculations should be highlighted: (i) the calculated magnitude of the steps at both T_R and T_N compare favorably with the measured values. In particular, for the $H_{\|c}$ case, the model reproduces clearly the monotonic field-induced decrease of the step size at T_R, while for the $H_{\|a}$ case, the model reproduces (though exaggeratedly) the three-events structure at $H=20$ kOe (see the bottom-left inset of Fig. 1); (ii) the surge of an anisotropy for the *spherical* $^{7/2}S$ Gd-moments even at temperatures as high as 20 K is well accounted for; and (iii) the reorientation process at T_R (along both field orientations) is shown to be a consequence of the joint action of exchange interactions and dipolar forces even though the energy of the former is at least five times larger than that of the latter: isotropic bilinear interaction, alone by themselves, do not lead to any reorientation processes. [35,29,36] Evidently in spite of the above-mentioned successes, this mean-field model calculations do not match quantitatively all the measured data and are not expected to account for the magnetic features of the specific heat within the very low-temperatures or in the neighborhood of T_N (the critical region).

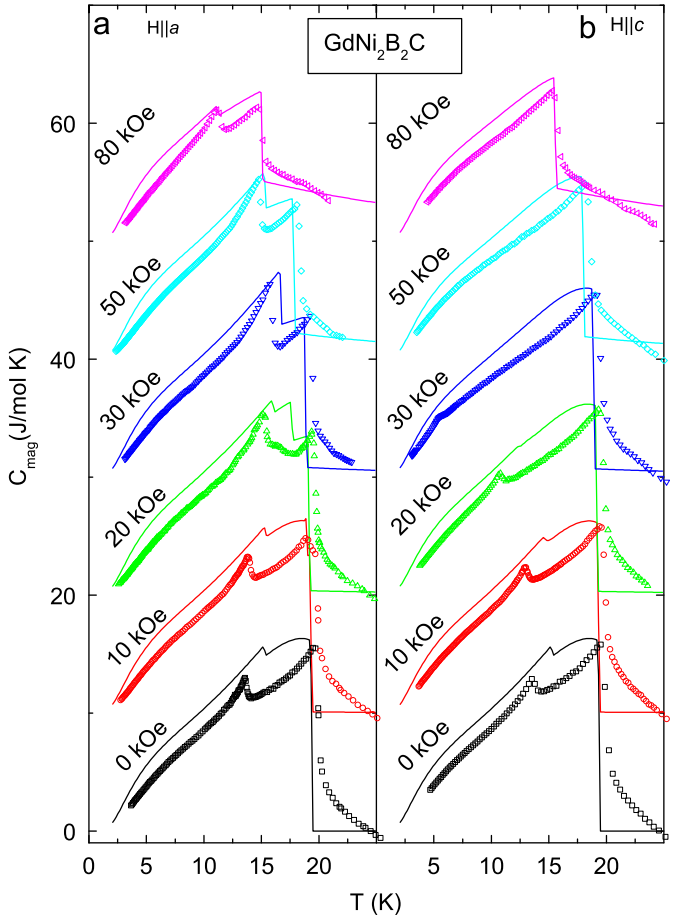

Fig. 3. Comparison of the calculated (solid lines) and measured (symbol) field-dependent magnetic specific heat of $GdNi_2B_2C$ for (a) $H\|a$ *axis* and (b) $H\|c$ *axis*. For ease of visualization, the successive curves are displaced upwards with the same amount of vertical shift (10 J/mol K). The calculations (with no adjustable parameters other than the experimental T_N) are based on the model proposed by Jensen and Rotter [7] (see text).

4.3.2. $ErNi_2B_2C$

The magnetic phase diagram of $ErNi_2B_2C$ is shown in the inset of Fig. 4 [16]: in zero field, this compound superconducts at 10.5 K and orders at $T_N=6.4$ K into an incommensurate modulated AFM structure with $k=(0.55,0,0)$ and moments pointing along the

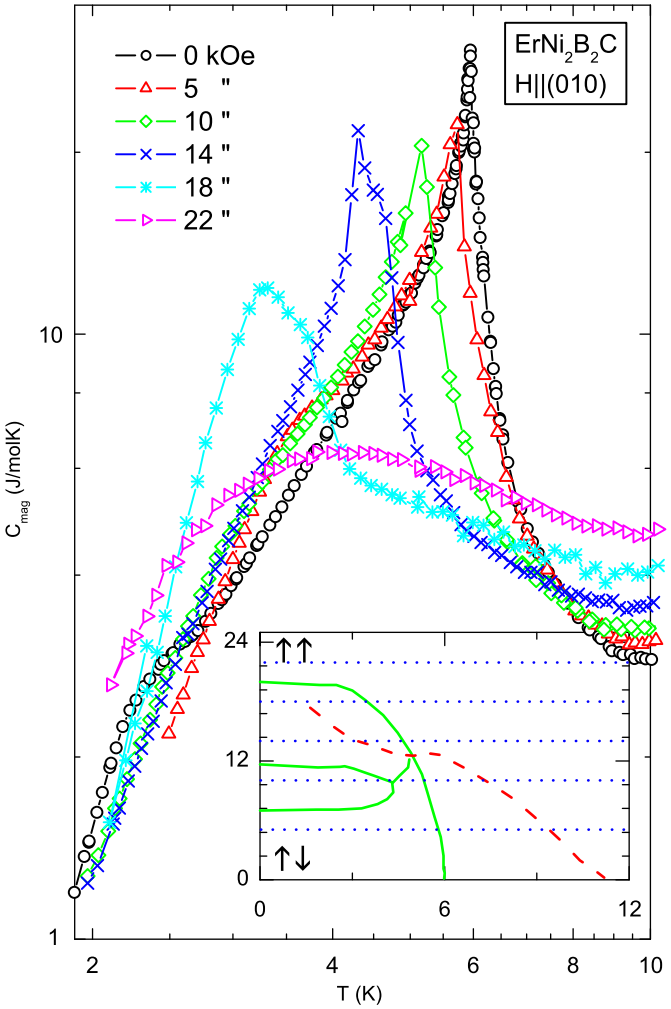

Fig. 4. (Color online) Thermal evolution of $C_{mag}(T,H)$ of $ErNi_2B_2C$ at various magnetic fields. The inset shows the H–T phase diagram (adapted from Ref. [16]): the thick dashed line represents the $H_{c2}(T)$—superconductivity—curve while the solid lines represent the various magnetic transformations. The horizontal dotted lines represent the magnetic fields that were applied during this study.

b-axis [37]. Below $T_{WFM} = 2.2$ K, a weak ferromagnetic (WFM) state [14] emerges together with an equal-amplitude, squared-up state [38,39]. A series of field-induced metamagnetic transformations appears when a field ($H < H_{sat}$) is applied along the easy axis (0,1,0) [10,16,40,17]: at 2 K, three metamagnetic transformations occur at 4, 11, and 20 kOe. For $H > H_{sat}$, the paramagnetic saturated state is stabilized.

To investigate the H- and T-dependence of $C_{mag}(T,H)$ across such a phase diagram, we carried out a series of isofield measurements with $H\|(0,1,0)$. The resulting $C_{mag}(T,H_{\|a})$ curves are shown in Fig. 4. The temperature dependence of the zero-field entropy (not shown) suggests that the lowest four level are fully populated above 10 K; this result is in agreement with the findings of Gasser et al. [41] that the electronic ground state is a doublet which is separated from the immediate excited state (also a doublet) by $0.6 \sim 0.7$ meV.

For $T < T_{WFM}(H < H_1)$, the zero-field magnetic sate is approximated as an AFM structure (see Section 2.1); accordingly, the measured $C_{mag}(T < T_{WFM}, H < H_1)$ curves are confronted with Eq. (1). Fig. 5 shows the excellent fit of $C_{mag}(T, H = 0\,\text{kOe})$ which gives $\Delta_a = 7.0 \pm 0.1$ K and $D = 3.0 \pm 0.1$ K. Using these parameters, we calculated the field-dependent $C_{mag}(T,H)$ curves (see Fig. 5). Once more, one observes the collapse of the $C_{mag}(T < T_{WFM}, H < H_1)$ curves within the immediate neighborhood of T^{-}_{WFM}. Due to experimental limitations, we were unable to probe the field evolution of $C_{mag}(T,H)$ for $T < T_{WFM}$ nor its temperature dependence for $H > H_{sat}$.

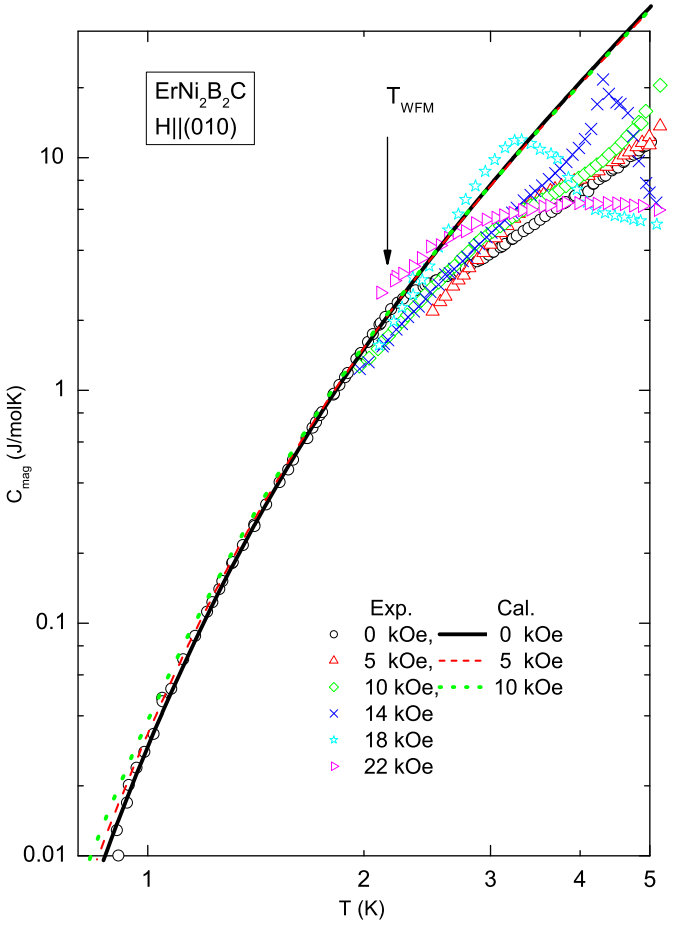

Fig. 5. (Color online) A log–log plot of the $C_M(T,H)$ curves of $ErNi_2B_2C$ at various applied magnetic fields. The magnetic specific heat (symbol) are compared with the theoretical calculation (lines) based on Eq. (1) (see text). The calculated curves of $H = 0, 5, 10$ kOe are different from each other only at $T < \Delta$.

4.3.3. $HoNi_2B_2C$

The magnetic specific heat of $HoNi_2B_2C$, reported by various groups (see e.g. [13,18,42,43]) reproduces faithfully the features of the magnetic phase diagram (in particular those incommensurate modes cited in Introduction) [13,15]. The main features of these $C_{mag}(T,H)$ curves can be comprehended in the light of Eq. (6b) and the evolution of the $M(T,H)$ curves [13]. Specifically, the overall features of the isofield $C_{mag}(T < 5\,\text{K}, H\|(1,0,0) < H_1)$, i.e. within the low-$T$ collinear AFM state [18], are well reproduced by Eq. (1): on reanalysis, the best fit parameters for the measured $C_{mag}(T, H = 0)$ were found to be $\Delta_a = 7.7 \pm 0.3$ K and $D = 4.6 \pm 0.2$ K.

5. Discussion and summary

The general evolution of $C_{mag}(T,H)$ within the magnetically ordered state of representative RNi_2B_2C (R = Gd, Ho, Er) is found to reflect faithfully the characteristic features of their H–T phase diagrams [13–16]. This is not surprising since the following Maxwell equations relate the evolution of $M(T,H)$ (based on which most of these phase diagrams were built) to that of $C_{mag}(T,H)$:

$$(\partial S_{mag}/\partial H)_T = (\partial M/\partial T)_H \tag{6a}$$

$$(\partial C_{mag}/\partial H)_T = T(\partial^2 M/\partial T^2)_H. \tag{6b}$$

It is worth adding that similar characteristic phase diagram features are evident also in many other magnetic properties such as the integrated intensities of the magnetic neutron diffractograms [10,11], the magnetostriction [17,26], and the magnetoresistivity [44,45].

One of the characteristic features of the magnetic phase diagrams is the stair-like behavior observed in the magnetization isotherms: it is assuring that this feature is manifested also in the $C_{mag}(T,H)$ case. Thus all $C_{mag}(T,H)$ curves that are within the same metamagnetic mode do collapse on each other (see e.g. inset of Fig. 3 in Ref. [18]). This feature is related to the contribution of the elementary magnetic excitations to the thermodynamical properties and here, in this work, we discuss this contribution in terms of the linearized spin-wave model (see the theory in Section 2.1 and its confrontation with the measured $C_{mag}(T,H)$ curves in Section 4.3)

Based on the analysis of Section 4 one is able to delineate the low-field, low-temperature range of the H–T phase diagrams wherein the linearized magnon contribution is found to describe satisfactory the experimental results: for $GdNi_2B_2C$, it is the $H < H_R(T)$ range wherein the sine-modulated state is squared-up; for $ErNi_2B_2C$ it encompasses the $H < H_1(T < T_{WFM})$ range wherein the squared-up AFM-like state is established; and finally for $HoNi_2B_2C$, it is the $H < H_1$ ($T < T_N$) range wherein the collinear AFM structure is established. In all these magnetic states, the magnetic specific heat is expressed by Eq. (1): the satisfactorily agreements between the calculated and measured $C_{mag}(T,H)$ justifies the assumptions considered in this model.

The values of the fit parameters evolves reasonably well across the studied compounds: as an example, the gap parameter of $GdNi_2B_2C$ ($\Delta_a = 2.9$ K) is much smaller than the corresponding values of $HoNi_2B_2C$ ($\Delta_a = 7.7$ K) and $ErNi_2B_2C$ ($\Delta_a = 7.0$ K); based on Eq. (3), such a result does agree with the well-established fact that the anisotropic field for $GdNi_2B_2C$ is extremely small. On the other hand, the stiffness constant of $GdNi_2B_2C$ ($D = 5.5$ K) is greater than that of $HoNi_2B_2C$ ($D = 4.6$ K) and $ErNi_2B_2C$ ($D = 3.0$ K); based on Eq. (2), this is related to the fact that the effective exchange couplings of $GdNi_2B_2C$ (proportional to the de Gennes factor) are the strongest. It is recalled that no direct scaling with the de Gennes factor should be expected since D given by Eq. (2) contains also H_a.

As the investigated compounds are good representatives of the other magnetic borocarbides, then it is expected that the above mentioned characteristic step-like behavior should be manifested also in other magnetic RNi_2B_2C compounds: indeed, the $M(T,H)$ isotherms of $TbNi_2B_2C$ (having similar anisotropic features as those of $ErNi_2B_2C$) manifest such a stair-like feature [40,46,47]. Then, based on Eq. (6b), its $C_{mag}(T,H)$ features should be similar to those of the studied compounds. It is emphasized that the manifestation of such stair-like features is a more general property since it is manifested, not only in the $M(T,H)$ isotherms, but also in several other thermodynamical quantities (see above). Accordingly such a generality suggests that, although other models have been applied to analyze these stair-like features in, e.g., $HoNi_2B_2C$ (Refs. [4,5]) and $ErNi_2B_2C$ [8], an analysis in terms of the spin-wave model is shown to be extremely useful for the description of the low-temperature thermodynamical properties of these magnetic compounds.

Acknowledgments

We acknowledge the partial financial support from the Brazilian agencies CNPq (485058/2006-5) and Faperj (E-26/171.343/2005) and the Austrian Science Foundation (FWF) P16250.

References

[1] K.-H. Müller, V.N. Narozhnyi, Rep. Prog. Phys. 64 (2001) 943.
[2] P.C. Canfield, P.L. Gammel, D.J. Bishop, Phys. Today 51 (1998) 40.
[3] B.K. Cho, P.C. Canfield, D.C. Johnston, Phys. Rev. Lett. 77 (1996) 163.
[4] V.A. Kalatsky, V.L. Pokrovsky, Phys. Rev. B 57 (1998) 5485.
[5] A. Amici, P. Thalmeier, Phys. Rev. B 57 (1998) 10684.
[6] M. Rotter, A. Schneidewind, M. Doerr, M. Loewenhaupt, M. El Massalami, C. Detlefs, Physica B 345 (2004) 231.
[7] J. Jensen, M. Rotter, Phys. Rev. B 77 (2008) 134408.
[8] J. Jensen, Phys. Rev. B 65 (2002) 140514(R).
[9] J.W. Lynn, S. Skanthakumar, Q. Huang, S.K. Sinha, Z. Hossain, L.C. Gupta, R. Nagarajan, C. Godart, Phys. Rev. B 55 (1997) 6584.
[10] A.J. Campbell, D.M. Paul, G.J. MacIntyre, Solid State Commun. 115 (2000) 213.
[11] A.J. Campbell, D.M. Paul, G.J. McIntyre, Phys. Rev. B 61 (2000) 5872.
[12] C. Detlefs, F. Bourdarot, P. Burlet, P. Dervenagas, S.L. Bud'ko, P.C. Canfield, Phys. Rev. B 61 (2000) 14916.
[13] P.C. Canfield, B.K. Cho, D.C. Johnston, D.K. Finnemore, M.F. Hundley, Physica C 230 (1994) 397.
[14] P.C. Canfield, S.L. Bud'ko, B.K. Cho, Physica C 262 (1996) 249.
[15] P.C. Canfield, S.L. Bud'ko, B.K. Cho, A. Lacerda, D. Farrell, E. Johnston-Halperin, V.A. Kalatsky, V.L. Pokrovsky, Phys. Rev. B 55 (1997) 970.
[16] S.L. Bud'ko, P.C. Canfield, Phys. Rev. B 61 (2000) R14932.
[17] M. Doerr, M. Rotter, M. El Massalami, S. Sinning, H. Takeya, M. Loewenhaupt, J. Phys.: Condens. Matter 14 (2002) 5609.
[18] M. El Massalami, H. Takeya, C.M. Chaves, Phys. Rev. B 70 (2004) 014429.
[19] M. El Massalami, R.E. Rapp, F.A.B. Chaves, H. Takeya, C.M. Chaves, Phys. Rev. B 67 (2003) 224407.
[20] R.J. Joenk, Phys. Rev. 128 (1962) 1634.
[21] C. Kittel, Quantum Theory of Solids, Wiley, New York, 1963.
[22] M. Rotter, A. Lindbaum, A. Barcza, M. El Massalami, M. Doerr, M. Loewenhaupt, H. Michor, B. Beuneu, Europhys. Lett. 75 (2006) 160.
[23] M. Rotter, J. Magn. Magn. Mater. 272–276 (2004) 481.
[24] B.K. Cho, P.C. Canfield, L.L. Miller, D.C. Johnston, W.P. Beyermann, A. Yatskar, Phys. Rev. B 52 (1995) 3684.
[25] P.C. Canfield, B.K. Cho, D.C. Johnston, Physica B 215 (1995) 337.
[26] M. El Massalami, H. Takeya, K. Hirata, M. Amara, R.-M. Galera, D. Schmitt, Phys. Rev. B 67 (2003) 144421.
[27] H. Takeya, T. Hirano, K. Kadowaki, Physica C 256 (1996) 220.
[28] M. El Massalami, R.E. Rapp, H. Takeya, in: A. Narlikar (Ed.), Studies in High Temperature Superconductors, vol. 45, Nova Science, New York, 2003, p. 153.
[29] M. Bouvier, P. Lethuillier, D. Schmitt, Phys. Rev. B 43 (1991) 13137.
[30] H. Michor, T. Holubar, C. Dusek, G. Hilscher, Phys. Rev. B 52 (1995) 16165.
[31] M. Kruis, G.R. Pickett, M.C. Veuro, Phys. Rev. B 177 (1969) 910.
[32] M. Kruis, G.R. Pickett, M.C. Veuro, Solid State Commun. 14 (1974) 191.
[33] C. Detlefs, A.I. Goldman, C. Stassis, P.C. Canfield, B.K. Cho, J. Hill, D. Gibbs, Phys. Rev. B 53 (1996) 6355.
[34] K. Tomala, J.P. Sanchez, P. Vulliet, P.C. Canfield, Z. Drzazga, A. Winiarska, Phys. Rev. B 58 (1998) 8534.
[35] J.A. Blanco, D. Gignoux, D. Schmitt, Phys. Rev. B 43 (1991) 13145.
[36] M. Rotter, M. Loewenhaupt, M. Doerr, A. Lindbaum, H. Michor, Phys. Rev. B 64 (2001) 014402.
[37] J.W. Lynn, S. Skanthakumar, Q. Huang, S.K. Sinha, Z. Hossain, L.C. Gupta, R. Nagarajan, C. Godart, Phys. Rev. B 55 (1997) 6584.
[38] H. Kawano-Furukawa, H. Takeshita, M. Ochiai, T. Nagata, H. Yoshizawa, N. Furukawa, H. Takeya, K. Kadowaki, Phys. Rev. B 65 (2002) 180508(R).
[39] S.-M. Choi, J.W. Lynn, D. Lopez, P.L. Gammel, P.C. Canfield, S.L. Bud'ko, Phys. Rev. Lett. 87 (2001) 107001.
[40] P.C. Canfield, S.L. Bud'ko, J. Alloys Compd. 262–263 (1997) 169.
[41] U. Gasser, P. Allenspach, F. Fauth, W. Henggeler, J. Mesot, A. Furrer, S. Rosenkranz, P. Vorderwisch, M. Buchgeiste, Z. Phys. B 101 (1996) 345.
[42] M. El-Hagary, H. Michor, C. Jambrich, R. Hauser, M. Galli, E. Bauer, G. Hilscher, J. Magn. Magn. Mater. 177–181 (1995) 551.
[43] S. Miyamoto, H. Takeya, K. Kadowaki, Physica C 282–287 (1997) 1409.
[44] M. El Massalami, E. Baggio-Saitovitch, J. Magn. Magn. Mater. 153 (1996) 97.
[45] I.R. Fisher, J.R. Cooper, P.C. Canfield, Phys. Rev. B 56 (1997) 10820.
[46] B.K. Cho, P.C. Canfield, D.C. Johnston, Phys. Rev. B 53 (1996) 8499.
[47] M. El Massalami, M. Amara, R.-M. Galera, D. Schmitt, H. Takeya, Phys. Rev. B 76 (2007) 104410.